Impact of Stoichiometry on the Hydrogen Storage Properties of $LiNH_2-LiBH_4-MgH_2$ Ternary Composites

Andrea Sudik,*,† Jun Yang,† Donald J. Siegel,† C. Wolverton,‡ Roscoe O. Carter III.,† and A. R. Drews†

Ford Motor Company, Research and Advanced Engineering, MD1170/RIC, P.O. Box 2053, Dearborn, Michigan 48121, and Materials Science and Engineering Department, Northwestern University, 2220 Campus Drive, Evanston, Illinois 60208

Received: August 14, 2008; Revised Manuscript Received: November 21, 2008

We recently reported (Yang, J.; et al. *Angew. Chem., Int. Ed.* **2008**, *47*, 882) a novel hydrogen storage composite involving a 2:1:1 $LiNH_2$:$LiBH_4$:MgH_2 ratio. On the basis of in-depth experimental and computational analysis, this composite was found to release hydrogen via a complex multistep reaction cascade, which seeded the products of a subsequent reversible hydrogen storage reaction. This so-called autocatalytic reaction sequence was found to result in favorable kinetics, ammonia attenuation, and partial low-temperature reversibility. Here, we extend our original study by examining the effects of reactant stoichiometry on the ensuing hydrogen storage desorption pathway and properties. In particular, we examine four $(LiNH_2)_X-(LiBH_4)_Y-(MgH_2)_Z$ composites, where $X:Y:Z = 2:1:2$, 1:1:1, 2:0.5:1, and 2:1:1 (original stoichiometry). For each sample, we characterize the postmilled mixtures using powder X-ray diffraction (PXRD) and infrared spectroscopy (IR) analyses and observe differences in the relative extent of two spontaneous milling-induced reactions. Variable-temperature hydrogen desorption data subsequently reveal that all composites exhibit a hydrogen release event at rather low temperature, liberating between 2.3 (1:1:1) and 3.6 (2:0.5:1) wt % by 200 °C. At higher temperatures (200−370 °C), the hydrogen release profiles differ considerably between composites and release a total of 5.7 (1:1:1) to 8.6 (2:0.5:1) wt %. Utilizing variable-temperature IR and PXRD data coupled with first-principles calculations, we propose a reaction pathway that is consistent with the observed phase progression and hydrogen desorption properties. From these data, we conclude that premilled reactant stoichiometry has a profound impact on reaction kinetics and high-temperature reaction evolution because of reactant availability. From this enhanced understanding of the desorption process, we recommend and test a stoichiometrically optimal ratio (3:1:1.5) which releases a total of 9.1 wt % hydrogen. Finally, we assess the reversibility (at 180 °C) of the four primary composites over two desorption cycles and find that only the 2:1:1 and 2:0.5:1 are reversible (3.5 wt % for 2:0.5:1).

1. Introduction

Safe and efficient on-board hydrogen storage is widely recognized as an enabling technology for the advancement of hydrogen-fueled vehicles.[1] While there are several challenges associated with the development of a viable hydrogen storage system (including issues such as cost and durability) for automotive applications where size and weight are constrained, volumetric and gravimetric hydrogen densities are of particular concern. As an example, even though hydrogen gas at STP has approximately three times the energy density of gasoline by weight, its volumetric energy density when compressed to 700 bar is only ∼15% of that of gasoline. Moreover, accounting for the weight and volume penalties associated with the tank and ancillary components required for containment, current high-pressure storage systems (350−700 bar) achieve densities of only 3−4 wt % H_2 and ∼20 g of H_2/L, which is far below the density of a gasoline fuel system as well as the targets established by the U.S. Department of Energy.[2] Consequently, breakthroughs for further densification of hydrogen are highly desirable.

Perhaps the most promising approach to achieving automotive hydrogen storage targets is via materials-based storage. Complex hydrides are one class of material which has been proposed for storage applications. These materials, optimally composed of lightweight cations and hydrogen-containing complex anions such as borohydrides (BH_4^-)[3−5] and alanates (AlH_4^-),[6,7] show promise for hydrogen storage as they are theoretically capable of achieving both high volumetric and gravimetric hydrogen densities (e.g., $LiBH_4$ contains 18.5 wt % H_2 and 120 g of H_2/L). Nevertheless, the strong bonding of hydrogen in complex hydrides typically requires high temperatures and/or low pressures to liberate hydrogen from these very stable materials. In addition, at temperatures of practical interest, storage reactions involving complex hydrides frequently release hydrogen at prohibitively slow rates (poor kinetics).

In an attempt to remedy these deficiencies, several approaches for improving the thermodynamic and kinetic properties of complex hydrides have been explored. These include "destabilized" reactions (e.g., $LiBH_4-MgH_2$),[8−11] catalyzed reactions (e.g., $TiCl_3-NaAlH_4$),[12,13] and discovery of new complex hydride reactants [e.g., $Li_4(NH_2)_3(BH_4)$][14−16] and products [e.g., $Li_2Mg(NH)_2$].[17,18] Building on this work, we recently presented a method for further enhancing the properties of complex hydrides through an "autocatalyzed" multistep reaction path-

* To whom correspondence should be addressed. E-mail: asudik@ford.com.
† Ford Motor Company.
‡ Northwestern University.

10.1021/jp807270y CCC: $40.75
Published on Web 01/13/2009

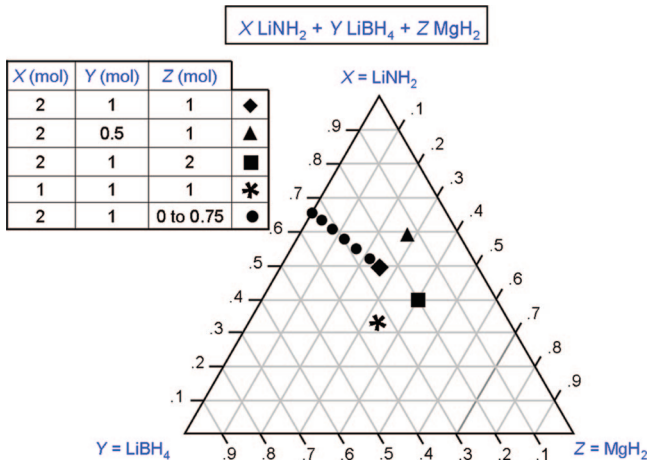

Figure 1. Ternary phase space bounded by unary compounds, $LiNH_2$ (*X*), $LiBH_4$ (*Y*), and MgH_2 (*Z*). The present study pertains to $(LiNH_2)_X$−$(LiBH_4)_Y$−$(MgH_2)_Z$ composites where *X*:*Y*:*Z* = 1:1:1 (star), 2:1:2 (square), 2:0.5:1 (triangle), and 2:1:1 (diamond). For reference, $(LiNH_2)_2$−$LiBH_4$−$(MgH_2)_Z$ compositions from a previous study (ref 20), where *Z* = 0−0.75 (circles), are also depicted.

way.[19] Specifically, a combination of three hydride compounds, a 2:1:1 molar ratio of $LiNH_2$, $LiBH_4$, and MgH_2, was found to exhibit a reduced desorption temperature (∼140 °C onset), increased H_2 purity, facile kinetics, and partial reversibility (2.8 wt % at 140 °C) as compared to its individual constituents. In-depth phase identification, property analysis, and first-principles calculations revealed that these properties arose via a coupled reaction cascade, yielding an autocatalyzed reversible hydrogen desorption step. More recently, a follow-up study was conducted to evaluate the role of MgH_2 in the multistep hydrogen storage process.[20] On the basis of a series of $(LiNH_2)_2$−$LiBH_4$−$(MgH_2)_Z$ compositions (where *Z* = 0−1), the desired autocatalyzed reaction pathway was increasingly accessed (and hydrogen storage properties improved) for increasing amounts of MgH_2 (maximized at *Z* = 1). A related study probing the impact of small amounts of $LiBH_4$ on $Mg(NH_2)$−LiH (1:2) was also recently reported by Hu et al.[21] However, these studies did not examine the effect of variable amounts of $LiNH_2$ and/or larger fractions of $LiBH_4$ (including MgH_2 amounts beyond 33 mol %).

To further clarify the impact of reactant stoichiometry on the properties of the ternary composites $(LiNH_2)_X$−$(LiBH_4)_Y$−$(MgH_2)_Z$, herein we report the synthesis, characterization, hydrogen storage characteristics, and hydrogen desorption pathway for composites having stoichiometric ratios of *X*:*Y*:*Z* = 1:1:1, 2:1:2, 2:0.5:1, and 2:1:1 (the 2:1:1 composition was previously reported in ref 19 and is included here to facilitate comparisons). The location of these composites on the $LiNH_2$−$LiBH_4$−MgH_2 ternary phase diagram is depicted in Figure 1. Compositions from the variable MgH_2 study [i.e., $(LiNH_2)_2$−$LiBH_4$−$(MgH_2)_Z$, where *Z* = 0−0.75] in ref 20 have also been included in Figure 1 for comparison. Additionally, a related combinatorial synthesis and screening investigation has also been completed for $LiNH_2$−$LiBH_4$−MgH_2 composites at all intersecting grid points of the Figure 1 phase diagram.[22] The primary scope of this high-throughput study was to efficiently screen reversible hydrogen capacity under a specific set of temperature and pressure conditions. The study did not include detailed characterization of the reaction pathway for each stoichiometry, an important exercise for future optimization of the $LiNH_2$−$LiBH_4$−MgH_2 ternary phase space.

In the present study, we first characterize the relative extents of two spontaneous milling-induced reactions for the 1:1:1, 2:1:2, 2:0.5:1, and 2:1:1 composites using powder X-ray diffraction (PXRD) and infrared spectroscopy (IR). The variable-temperature hydrogen desorption behavior for postmilled compositions is subsequently examined, revealing that all composites release hydrogen via multistep processes. In general, the behavior of all compositions can be grouped into three phases: (i) initial low-temperature milling reactions, (ii) low-to-moderate-temperature hydrogen releasing reactions, and (iii) high-temperature hydrogen releasing reactions. At low temperatures (i), all composites share the same initial non-hydrogen releasing reactions, suggesting that these steps occur independently of the starting stoichiometry (albeit to different extents). As the temperature is raised (ii), moderate differences in the hydrogen releasing properties of the composites begin to emerge. Nevertheless, all composites exhibit hydrogen releasing events at rather low temperatures, for example, liberating between 2.3 (1:1:1) and 3.6 (2:0.5:1) wt % by 200 °C. Finally, at higher temperatures (iii) between 200 and 350 °C, the hydrogen releasing steps differ significantly between compositions and release a total of 5.7 (1:1:1) to 8.6 (2:0.5:1) wt %.

On the basis of in-depth variable-temperature PXRD and IR data as well as first-principles computational analysis, we suggest a set of consecutive reactions that is consistent with the observed phase evolution and hydrogen desorption behavior. From these data, we conclude that stoichiometry has a significant impact on reaction kinetics and the high-temperature reaction progression based on differences in reactant availability. Specifically, we reveal that composites that are $LiNH_2$-deficient and MgH_2-abundant (e.g., 2:1:2 and 1:1:1 contain 38 and 32 mol % $LiNH_2$ and 44 and 37 mol % MgH_2, respectively) follow a new high-temperature reaction sequence and share similar hydrogen storage properties. Conversely, composites that are $LiNH_2$-abundant and MgH_2-deficient (e.g., 2:1:1 and 2:0.5:1 contain 49 and 55 mol % $LiNH_2$ and 28 and 32 mol % MgH_2, respectively) react according to the desorption pathway originally proposed in ref 19. On the basis of these data, we discuss factors that may explain differences between these two sets of related compositions. We additionally suggest (and test) a new reactant ratio for the proposed reaction sequence that should be stoichiometrically optimum for simultaneously maximizing the reversible and overall hydrogen capacity (a 3:1:1.5 $LiNH_2$:$LiBH_4$:MgH_2 ratio). Incidentally, this ratio is quite close to the ratio (a 3:0.5:1.5 $LiNH_2$:$LiBH_4$:MgH_2 ratio) that exhibited the highest reversible capacity from the high-throughput screening study in ref 22. Finally, we evaluate the moderate-temperature (180 °C) reversible capacity for the four primary compositions over two cycles and find that only the 2:1:1 and 2:0.5:1 composites are reversible (e.g., 3.5 wt % reversible for 2:0.5:1).

2. Experimental Section

2.1. Sample Preparation. Lithium borohydride ($LiBH_4$) (95%, Sigma-Aldrich), magnesium hydride (MgH_2) (95%, Gelest), and lithium amide ($LiNH_2$) (95%, Sigma-Aldrich) were used as received. All sample handling was performed in an MBraun Labmaster 130 glovebox maintained under an argon atmosphere with <1 ppm O_2 and H_2O vapor levels. For each composition, a 2 g sample of $LiNH_2$, $LiBH_4$, and MgH_2 in a 1:1:1, 2:1:2, 2:1:1, or 2:0.5:1 molar ratio was placed in a stainless steel milling vial containing three stainless steel balls weighing 8.4 g each. Mechanical milling was carried out using a Spex 8000 high-energy mixer/mill for 5 h.

2.2. Kinetic Measurements. ***2.2.1. TPD-MS.*** Variable-temperature hydrogen desorption behavior was measured using

a temperature-programmed desorption (TPD) apparatus constructed in-house utilizing a MKS PPT electron-ionization quadrapole mass spectrometer (MS) equipped with a heated capillary inlet (115 °C), a Lindberg tube furnace with programmable temperature control, and a Brooks 5850 E-series mass flow controller. For each experiment, a specimen of approximately 20 mg of sample was loaded into a quartz tube between quartz wool plugs. The septum-sealed specimen tube was placed in the furnace, and a continuous flow of UHP Ar carrier gas (100 sccm flow rate) was passed through the specimen while it was heated at a programmed rate of 5 °C/min from room temperature to 370 °C. Concentrations of hydrogen ($m/z = 2$) and ammonia ($m/z = 17$) in the effluent were determined by comparison to single-point calibrations obtained using certified mixtures of 1% H_2/N_2 and 2.05% NH_3/N_2, and all TPD-MS comparison plots were normalized against the sample weight. The mass signals corresponding to a variety of non-hydrogen volatile or gaseous species (e.g., ammonia, diborane, borazine, water, oxygen, etc.) were also tracked during the TPD-MS experiments and, with the exception of ammonia, were found to remain below the detection limit of our instrument (100 ppm) throughout the entire temperature profile.

2.2.2. WDD. Variable-temperature hydrogen desorption kinetics were characterized using a water displacement desorption (WDD) apparatus constructed in-house where the desorbed gas amount was directly monitored as a function of temperature. For each experiment, approximately 250 mg of sample was loaded into a stainless steel autoclave. The sealed autoclave was mounted onto a three-port manifold connected to UHP Ar purge gas as well as an outlet tube that passes through the bottom of a water-filled graduated buret. The manifold and sample were purged with Ar prior to each experiment. The sample was heated at a constant rate (5 °C/min) from room temperature to the final set point (up to 370 °C), and the desorbed hydrogen volume was manually monitored as the amount of water is displaced in the buret. The amount of desorbed hydrogen was corrected for the reduced headspace pressure and thermal expansion of 1 bar of Ar gas upon sample heating.

2.2.3. PCT. Isothermal hydrogen desorption and cycling experiments were performed using a PCT Pro-2000 Sievert-type pressure−composition−temperature (PCT) apparatus from Hy-Energy. In a typical experiment, a 200 mg sample was loaded into an autoclave sample holder having a thermocouple that penetrates into the sample interior. Temperatures and pressures of the sample and gas reservoirs were monitored by LabView-based control software. Desorption kinetics were performed at the indicated temperature (180−250 °C) using hydrogen back pressure (1 bar). Adsorption experiments were performed at a 180 °C and 150 bar hydrogen pressure.

2.3. Characterization. ***2.3.1. In Situ Powder X-ray Diffraction (PXRD).*** Phase identity and purity was characterized by using variable-temperature in situ powder X-ray diffraction data collected using a Bueler HDK 2.4 furnace chamber attached to a Scintag X1 diffractometer, an Inel CPS 120 position sensitive detector, and collimated Cu Kα radiation. Specimens were prepared in an inert atmosphere glovebox by spreading powder onto a sapphire crystal with a drop of mineral oil impregnated into the powder and then stored in a sealed container to protect the powder against exposure to room air during transfer into the HTXRD chamber. Once the specimen was placed onto the heating strip, and the furnace chamber was sealed, the atmosphere inside the chamber was evacuated and backfilled with nitrogen several times to eliminate residual oxygen and moisture. Data were collected under an atmosphere of flowing purified nitrogen (200 sccm), while the temperature was ramped at a continuous rate of 2 °C/min from 50 to 300 or 350 °C, following an initial room-temperature scan. The residual mineral oil used during sample transfer and loading results in an observed halo at 20° (two-theta) in the two-dimensional contour plot data (Figure 4). This effect persists from room temperature to 100 °C at which point the mineral oil becomes less viscous and is able to flow off of the sample holder. Scans were integrated for 5 min, each corresponding to a temperature average over a 10 °C window while ramping. The phase assemblage was determined for each scan using the MDI JADE software and the Powder Diffraction File (PDF−4). In addition, the presence of transient liquid phases made a complete quantitative analysis impossible, and phase assemblages presented here are from tracking the net intensities of representative peaks for each crystalline phase.

2.3.2. In Situ Infrared Spectroscopy (IR). Variable-temperature diffuse reflectance infrared spectra were obtained on a Mattson Instruments Sirius 100 FT-IR spectrometer with upgraded electronics and high-speed parallel data transfer capability. The unit was equipped with a water-cooled source and a HgCdTe nitrogen-cooled detector. A Harrick praying mantis accessory with a high-temperature environmental cell was used, which was equipped with KBr windows. Finely ground KBr powder was used as a reference material. The instrument was purged with boil-off liquid nitrogen, while the sample cell was purged with flowing UHP helium. The interferometer mirror velocity corresponded to a HeNe modulation frequency of 40 kHz. All data manipulations and transformations were accomplished with Mattson WinFirst software. Each sample was heated at a rate of 5 °C/min from room temperature to 320 °C.

2.4. Density Functional Theory (DFT) Calculations. First-principles calculations of finite-temperature thermodynamic quantities, enthalpies, entropies, and free energies were performed using density functional theory (VASP[23] code), in conjunction with an evaluation of lattice normal-mode vibrational frequencies via the harmonic approximation. The projector augmented wave method[24] was used to describe the core−valence interaction, and the exchange-correlation energy was evaluated using the PW91 generalized gradient approximation.[25] The crystallographic phases used for DFT calculations on $LiNH_2$, $LiBH_4$, $Li_4BN_3H_{10}$, and Li_3BN_2 are described in ref 29. Sources for the structures of other relevant phases are as follows: $Mg(NH_2)_2$, ref 26; Mg_3N_2, ref 27; and α-$Li_2Mg(NH)_2$, ref 28. Further details regarding our calculations can be found elsewhere.[10,19,29,30]

3. Results and Discussion

3.1. Synthesis and Characterization of $(LiNH_2)_X$−$(LiBH_4)_Y$−$(MgH_2)_Z$ Composites. The four $(LiNH_2)_X$−$(LiBH_4)_Y$−$(MgH_2)_Z$ composites, where $X:Y:Z$ = 1:1:1, 2:1:2, 2:1:1, and 2:0.5:1, were prepared by milling the respective reactants in the appropriate molar ratios (section 2.1). The phase assemblage of the postmilled samples was subsequently characterized using PXRD (Figure 2a) and IR measurements (Figure 2b). From these data, it is evident that the premilled reactant stoichiometry has some impact on the identity and relative abundance of the phases present in the postmilled products. As previously reported for the 2:1:1 composite (pink, Figure 2), two new phases [$Li_4BN_3H_{10}$ and $Mg(NH_2)_2$] are observed in the postmilled sample. The identification of these phases is based on PXRD data as well as the observance of N−H amide stretches characteristic for $Li_4BN_3H_{10}$ (3303 and 3242 cm^{-1}, observed; 3303 and 3243 cm^{-1}, ref 31) and $Mg(NH_2)_2$ (3328 and 3272 cm^{-1}, observed;

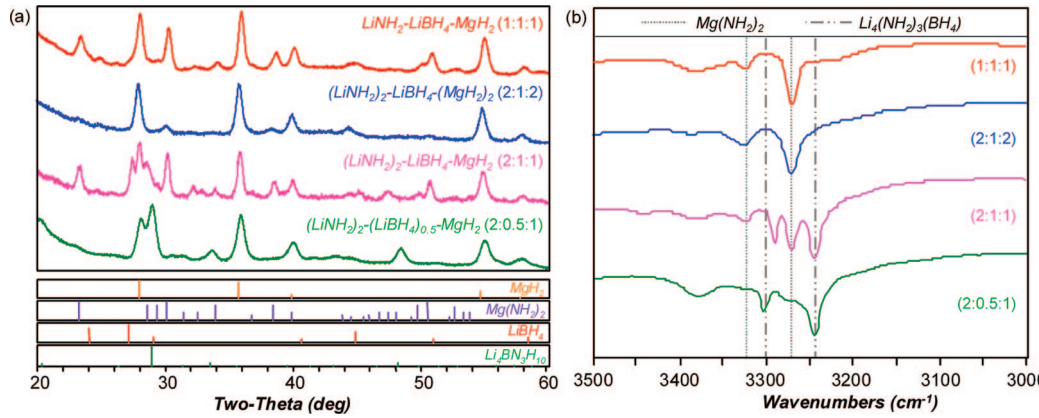

Figure 2. (a) Room-temperature PXRD patterns for ball-milled $(LiNH_2)_X$−$(LiBH_4)_Y$−$(MgH_2)_Z$ composites, where X:Y:Z = 1:1:1 (red), 2:1:2 (blue), 2:1:1 (pink), and 2:0.5:1 (green). Phase assignments were made based on comparisons with PDF data for MgH_2 (orange), $Mg(NH_2)_2$ (purple), and $LiBH_4$ (red) or patterns generated from samples prepared in-house, $Li_4BN_3H_{10}$ (green). (b) Room-temperature IR data (3500−3000 cm^{-1}) for samples in (a) (same color scheme used). Phase assignments were made based on comparisons with reference data for $Li_4BN_3H_{10}$ (ref 31) and $Mg(NH_2)_2$ (ref 32).

3325 and 3274 cm^{-1}, ref 32). We have previously concluded that these new species are produced through exothermic reactions 1 and 2:[19]

$$6LiNH_2 + 2LiBH_4 \rightarrow 2Li_4BN_3H_{10} \quad (1)$$

$$2Li_4BN_3H_{10} + 3MgH_2 \rightarrow 3Mg(NH_2)_2 + 2LiBH_4 + 6LiH \quad (2)$$

Reactions 1 and 2 are both exothermic, having reaction enthalpies (ΔH at 300 K) of −24 and −208 kJ, respectively. One could alternatively consider the formation of $Mg(NH_2)_2$ to occur through the sum of reactions 1 and 2, which is written as reaction 2a:

$$6LiNH_2 + 3MgH_2 + 2LiBH_4 \rightarrow 3Mg(NH_2)_2 + 6LiH + 2LiBH_4 \quad (2a)$$

which has a reaction enthalpy of −232 kJ. Thus there are at least two potential sequences that can be used to describe the formation of $Mg(NH_2)_2$, either reactions 1 and 2 or reaction 2a. That is, $Mg(NH_2)_2$ can be formed via $Li_4BN_3H_{10}$ and MgH_2 intermediates (reactions 1 and 2) or directly through reaction 2a (mediated by $LiBH_4$). To our knowledge, however, $Mg(NH_2)_2$ and LiH are not readily formed from ball milling $LiNH_2$ and MgH_2 (because of kinetic limitations).[32,33] Additionally, we have previously demonstrated reaction 2 between $Li_4BN_3H_{10}$ and MgH_2, in isolation.[19] These pieces of indirect information suggest reactions 1 and 2 are the observed routes of $Mg(NH_2)_2$ formation; however, additional in situ experiments are needed to confirm this postulation. In addition to these two new phases [$Li_4BN_3H_{10}$ and $Mg(NH_2)_2$], residual MgH_2 (but not $LiNH_2$) starting material is also detected for the postmilled 2:1:1 sample. For the 2:0.5:1 composite (green curves in Figure 2), $Li_4BN_3H_{10}$ is the majority phase (along with residual MgH_2), suggesting that reaction 1 has occurred to completion. However, the absence of the $Mg(NH_2)_2$ phase, a reaction 2 or 2a product, indicates that these reactions are largely absent after milling. Conversely, for both the 2:1:2 (blue) and 1:1:1 (red) composites, the majority products after milling are $Mg(NH_2)_2$ and MgH_2, with no apparent $Li_4BN_3H_{10}$. [The sharper diffraction peaks observed for the 1:1:1 sample suggest higher crystallinity for $Mg(NH_2)_2$.] Thus for these composites, reactions 1 and 2 (or 2a) have occurred to completion. The omission of reaction 2 (or 2a) in the 2:0.5:1 system suggests the presence of a kinetic barrier, limiting this reaction during milling where the temperature is limited. While we are unable to definitively explain this behavior, we note that the 2:0.5:1 mixture is unique in that it contains the largest proportion of $LiNH_2$ (55 mol %) of any stoichiometry. Likewise, the 2:1:1 mixture, which only partially completes reaction 2 (or 2a), exhibits the second highest proportion of the $LiNH_2$ reactant. The proportion of MgH_2 in these two mixtures is also lower than that in either the 2:1:2 or 1:1:1 system. On the basis of PXRD and IR data (Figure S1 in Supporting Information), initial heating of postmilled 2:1:1 and 2:0.5:1 samples to <110 °C (i.e., prior to H_2 release) proves successful for further promoting reaction 2, although not to completion. Thus, it is expected that after milling and initial heating (to <140 °C at 5 °C/min) the 2:1:2: and 1:1:1 composites largely contain $Mg(NH_2)_2$, LiH, MgH_2, and $LiBH_4$, whereas 2:1:1 and 2:0.5:1 composites contain the same species as well as some remaining $Li_4BN_3H_{10}$.[34]

3.2. Kinetic Desorption Behavior for Postmilled $(LiNH_2)_X$−$(LiBH_4)_Y$−$(MgH_2)_Z$ Composites. Variable-temperature WDD hydrogen desorption data and TPD-MS data were acquired in order to evaluate the kinetic desorption behavior for each composite stoichiometry. In both experiments, postmilled material was heated at 5 °C/min to 370 °C in a 1 bar (volumetric desorption) or 100 sccm flowing (TPD-MS) argon environment. These data are shown in the respective top and bottom panels of Figure 3. On the basis of our previous study,[19] the 2:1:1 composite (pink) releases hydrogen via a multistep desorption process and produces a total of 8.5 wt % hydrogen (top panel). The composition of the effluent gas for the 2:1:1 composite was also monitored by TPD-MS (bottom panel) with a hydrogen signal (m/z = 2) that begins at 140 °C and shows three distinct release events centered at 180, 190 (shoulder), and 310 °C.[35] Similar hydrogen desorption behavior is observed for the postmilled 2:0.5:1 composite (green). Specifically, the 2:0.5:1 composite has the same 140 °C desorption temperature onset and a total capacity of 8.6 wt %. The three-step desorption profile observed for 2:0.5:1 (maxima at 175, 190, and 305 °C) is virtually identical to that of the 2:1:1 composite. The overall similar hydrogen desorption behaviors for these two composites is understood as their pre- and postmilled phase compositions (section 3.1) were found to be comparable. There are only two notable differences between the 2:0.5:1 and 2:1:1 data. First, there is a change in the relative amount of hydrogen released during the low- vs high-temperature steps. In particular, the

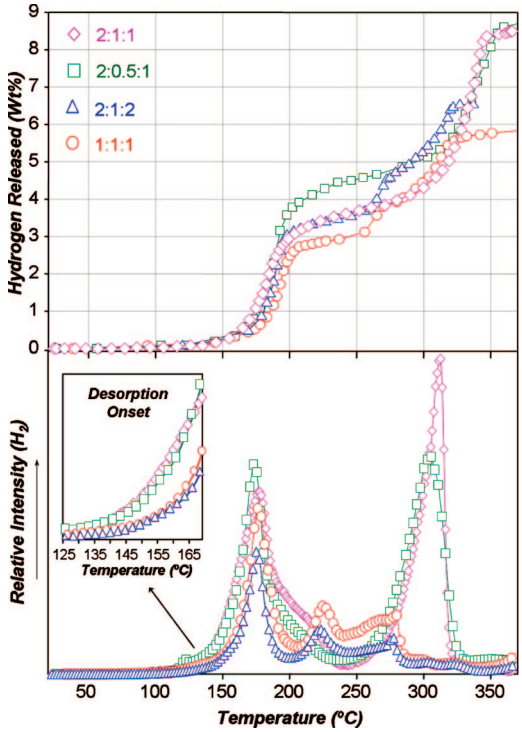

Figure 3. Kinetic hydrogen desorption data as a function of temperature (5 °C/min to 370 °C) for $(LiNH_2)_X-(LiBH_4)_Y-(MgH_2)_Z$ composites, where $X:Y:Z = 1:1:1$ (red circles), 2:1:2 (blue triangles), 2:1:1 (pink diamonds), and 2:0.5:1 (green squares). Top: Volumetric hydrogen desorption is given in weight percent (wt %) to 1 bar. Bottom: Temperature-programmed desorption mass spectrometry (TPD-MS) data for hydrogen ($m/z = 2$) are reported as relative partial pressure in a flow-through setup (100 sccm Ar). The bottom inset depicts TPD-MS data expanded over the 125−170 °C temperature range. TPD-MS data for ammonia ($m/z = 17$) can be found in Figure S2 of the Supporting Information.

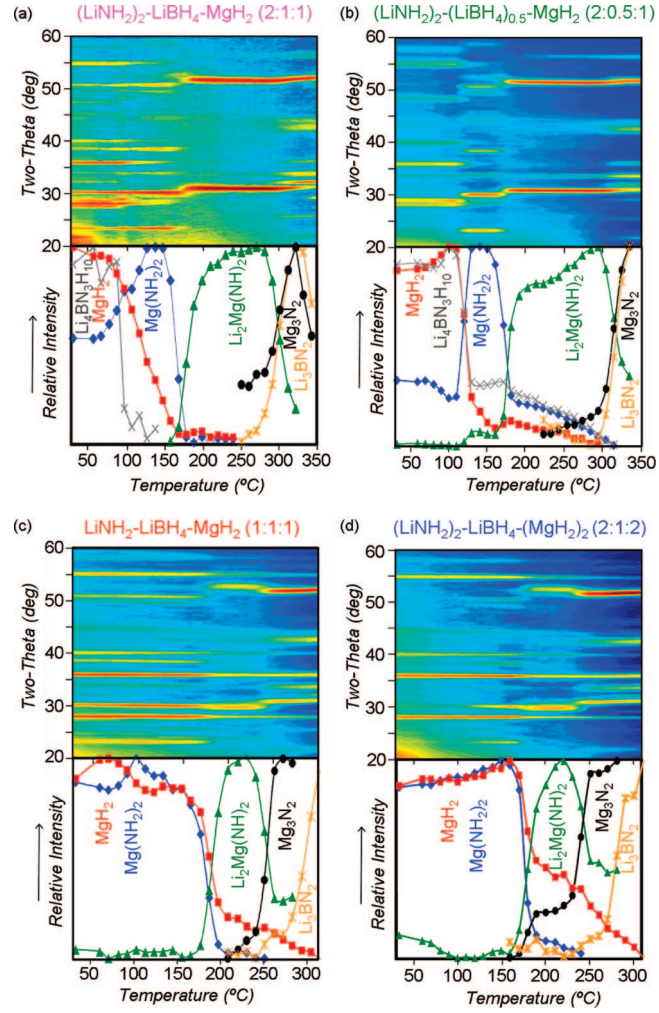

Figure 4. Powder X-ray diffraction (PXRD) data for $(LiNH_2)_X-(LiBH_4)_Y-(MgH_2)_Z$ composites as a function of temperature (25−350 °C), where $X:Y:Z =$ (a) 2:1:1 (pink), (b) 2:0.5:1 (green), (c) 1:1:1 (red), and (d) 2:1:2 (blue). The top panel in each plot is the two-dimensional contour plot derived from the raw patterns (Figures S3−S6 in the Supporting Information), whereas the bottom panel is a graph of the relative amounts of individual phases as a function of temperature.

2:0.5:1 composite liberates more hydrogen during the low-temperature steps (4.5 wt % at 250 °C) and less at the high-temperature step (8.6 wt % total) than compared to that of the 2:1:1 composite (3.7 wt % at 250 °C and 8.5 wt % total). (We compare observed and theoretical capacity data for all composites in sections 3.4 and 3.5.) Second, the amount of ammonia liberated (from 100 to 200 °C) for the 2:0.5:1 composite is almost an order of magnitude higher than that of the 2:1:1 sample (Figure S2 in Supporting Information). This enhancement in released ammonia could stem from the higher relative amide content [i.e., more $Li_4BN_3H_{10}$ and $Mg(NH_2)_2$] in the postmilled 2:0.5:1 composite vs the 2:1:1 composite. Potentially these amides are not as readily consumed (via reactions 2, 3, and 4), a kinetic effect leading to their self-decomposition which involves ammonia as a product.[28,36−38]

The remaining 2:1:2 (blue) and 1:1:1 (red) composites were determined to have similar pre- and postmilled phase compositions (section 3.1), and thus also exhibit similar desorption characteristics (Figure 3). The behavior for these two stoichiometries, however, is markedly different than that of the 2:0.5:1 and 2:1:1 composites described above. Specifically, 2:1:2 and 1:1:1 both possess significantly reduced total capacities, 6.6 and 5.7 wt % (top), respectively, as compared to that of the 2:0.5:1 and 2:1:1 mixtures. They also both release hydrogen in three distinct steps centered at 175, 225, and 275 °C with desorption onsets approximately 15 °C higher (at ∼155 °C) than that of the 2:1:1 and 2:0.5:1 composites (bottom). As will be discussed later, these higher onset temperatures for 2:1:2 and 1:1:1 are thought to stem from the absence of the kinetically enhancing product seeding step, which is observed in the 2:1:1 and 2:0.5:1 composites. While the peak of the low-temperature desorption step for 2:1:2 and 1:1:1 can largely be superimposed with that of the 2:0.5:1 and 2:1:1 composites, the two higher-temperature steps are noticeably different in terms of both peak position and magnitude. Finally, for both the 2:1:2 and 1:1:1 composites, there was negligible ammonia detected in the TPD-MS data (Figure S2 of Supporting Information) likely stemming from the low relative content and/or facile consumption of amide-based constituents. Overall, in Figure 3, it is evident that although the four composites are all based on the same initial reactants ($LiNH_2$, $LiBH_4$, and MgH_2), their specific reactant stoichiometry appears to impact both the phase composition after milling (under identical conditions) and the resulting desorption properties. Characterization of the desorption pathway for each composite will be used to better understand the effect of stoichiometry on the resulting properties.

3.3. Product Phase Analysis and Desorption Pathway Determination for Postmilled $(LiNH_2)_X-(LiBH_4)_Y-(MgH_2)_Z$ Composites. To understand the dependence of stoichiometry on the resulting desorption properties in the $(LiNH_2)_X-(LiBH_4)_Y-(MgH_2)_Z$ composites, it is necessary to fully charac-

terize each desorption pathway. From the previous study of the 2:1:1 mixture,[19] we found the task of deciphering the multistep reaction mechanism to be quite complex due to the large number of elements and reaction products having varying degrees of crystallinity. Similarly, on the basis of the observed multistep hydrogen release behavior in Figure 3, the remaining 2:0.5:1, 2:1:2, and 1:1:1 composites will require the same in-depth phase identification methods and first-principles calculations to elucidate the reaction details. In particular, we have employed both variable-temperature powder X-ray diffraction (PXRD) and variable-temperature infrared spectroscopy (IR) techniques to experimentally track product phases over the entire desorption temperature range (25−350 °C). The desorption pathway can be divided into two sets of hydrogen release reactions that occur at low (25−200 °C) and high (200−350 °C) temperatures. These reaction steps are described separately in sections 3.3.1 and 3.3.2, respectively.

3.3.1. Low-Temperature Hydrogen Release Steps. Figure 4 depicts results from the in situ PXRD analysis for each composite, specifically showing the two-dimensional contour plots (top panels) generated from raw data (Figures S3−S6 in the Supporting Information) and phase assemblage (bottom panels) as a function of temperature. On the basis of these data, which was previously collected for the postmilled 2:1:1 composite (Figure 4a), we had deduced[19] that the low-temperature hydrogen release steps, from 25 to 250 °C, involved the following reaction sequence:

$$2Li_4BN_3H_{10} + 3MgH_2 \rightarrow 3Mg(NH_2)_2 + 2LiBH_4 + 6LiH \quad (2b)$$

$$2Li_4BN_3H_{10} + 3MgH_2 \rightarrow 3Li_2Mg(NH)_2 + 2LiBH_4 + 6H_2 \quad (3)$$

$$3Mg(NH_2)_2 + 6LiH \leftrightarrow 3Li_2Mg(NH)_2 + 6H_2 \quad (4)$$

Specifically for the 2:1:1 composite, irreversible reaction 2, which was also observed upon milling (section 3.1), is further accessed during initial heating to 110 °C. This is evidenced by the disappearance of $Li_4BN_3H_{10}$ and MgH_2 phases in Figure 4a data where the former melts and reacts with the latter as well as the simultaneous emergence of the product $Mg(NH_2)_2$ phase. The presence of reaction 2 is further corroborated from new variable-temperature IR data which are depicted in Figure 5a for the 2:1:1 composite. In particular, the N−H amide stretches characteristic for $Li_4BN_3H_{10}$ (3303 and 3242 cm^{-1}, observed; 3303 and 3243 cm^{-1}, ref 31) disappear with a simultaneous growth in N−H amide stretches for $Mg(NH_2)_2$ (3328 and 3272 cm^{-1}, observed; 3325 and 3274 cm^{-1}, ref 32) between room temperature and 110 °C. As the temperature surpasses 110 °C, the remaining reactants ($Li_4BN_3H_{10}$ and MgH_2) undergo a second irreversible reaction 3, releasing hydrogen and forming $Li_2Mg(NH)_2$ and $LiBH_4$ product phases. This reaction 3 is supported by the appearance and growth of $Li_2Mg(NH)_2$ in both PXRD (Figure 4a) and IR data (Figure 5a; N−H stretch at 3178 cm^{-1}, observed and ref 36).

To corroborate the experimentally observed temperature at which reaction 3 becomes preferentially favored over reaction 2, the difference in total free energy (ΔG) for both reactions was computationally determined by density functional theory (DFT) over the full temperature profile (Figure 6). From these data, the calculated temperature at which the ΔG values for reactions 2 and 3 cross (i.e., reaction 3 becomes more negative than reaction 2) is approximately 170 °C, a temperature that is fairly consistent with the experimental observation of approximately 160 °C for kinetic desorption data (top panel, Figure 3), which is performed at 5 °C/min to 1 bar.[32] Incidentally, this temperature is also similar to that thermodynamically expected for reaction 4 (153 °C calculated temperature based on $\Delta H_{500\ K} = 47$ kJ/mol of H_2). Reaction 3 is crucial to the autocatalytic mechanism, as it serves to directly catalyze (or seed) the subsequent reversible reaction 4 between $Mg(NH_2)_2$ and LiH. More specifically, we believe reaction 3 preforms the product

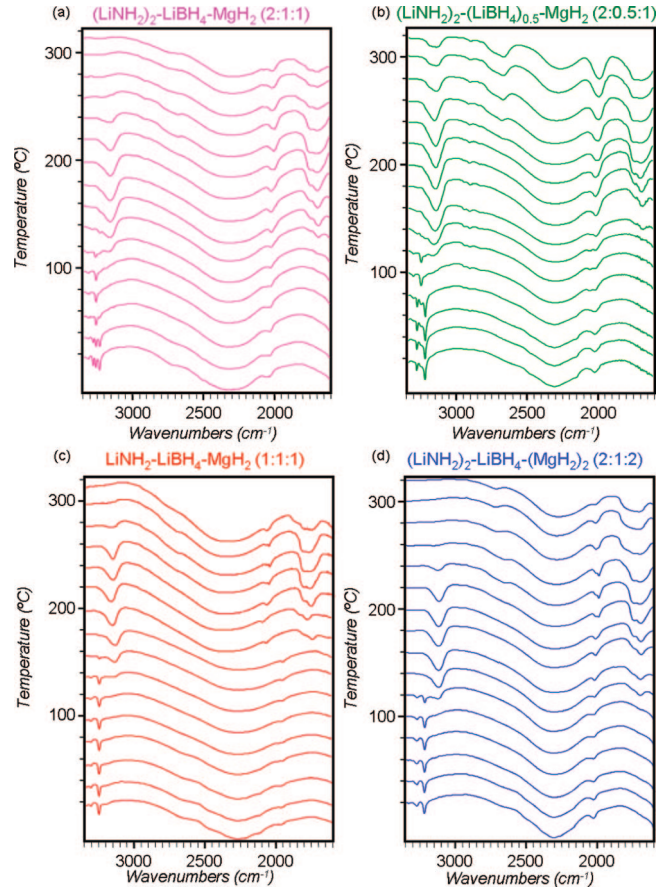

Figure 5. Infrared spectroscopy (IR) data for $(LiNH_2)_X-(LiBH_4)_Y-(MgH_2)_Z$ composites as a function of temperature (to 320 °C), where $X:Y:Z$ = (a) 2:1:1 (pink), (b) 2:0.5:1 (green), (c) 1:1:1 (red), and (d) 2:1:2 (blue). The spectra are expanded from 3350 to 1600 cm^{-1}. Phase assignments were made based on comparisons with reference data for $Li_4BN_3H_{10}$,[31] $Mg(NH_2)_2$,[32] $Li_2Mg(NH)_2$,[36] and Li_3BN_2.[39]

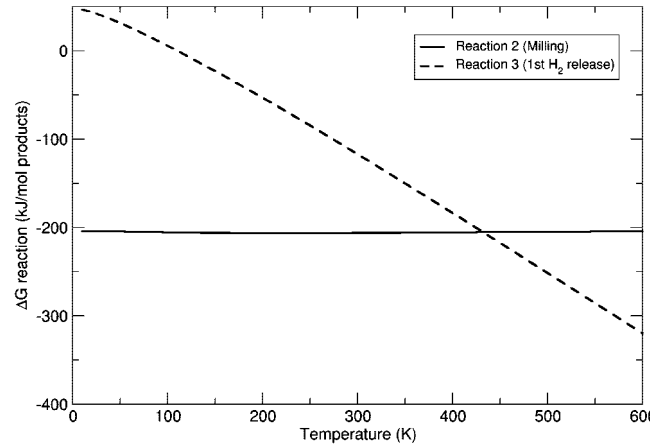

Figure 6. Difference in total free energy (ΔG) vs temperature (from 0 to 600 K) for reactions 2 and 3 computationally determined by density functional theory (DFT).

nuclei [$Li_2Mg(NH)_2$] for reaction 4, resulting in an enhancement in the overall kinetic properties.

On the basis of the in situ PXRD and IR data, the 2:0.5:1 composite (green, Figures 4b and 5b) behaves like the 2:1:1 composite for the low-temperature hydrogen release steps. Specifically 2:0.5:1 follows the same reaction 2−4 sequence as the 2:1:1 composite. The only variation between these composites concerns differences in their initial postmilled compositions (section 3.1). Specifically, the 2:0.5:1 postmilled composition is largely composed of $Li_4BN_3H_{10}$ and MgH_2 [with no obvious $Mg(NH_2)_2$]. Therefore, reaction 2 occurs solely during initial heating (at approximately 110 °C) for the 2:0.5:1 composite as shown by data in Figures 4b and 5b. Subsequent reactions 3 and 4 occur at essentially the same temperature as in the 2:1:1 composite, also resulting in the preferred autocatalytic mechanism for the 2:0.5:1 composite.

The phase evolution during desorption of postmilled 2:1:2 and 1:1:1 composites differs considerably over the low-temperature region (25−200 °C) than that described for the 2:1:1 and 2:0.5:1 compositions. As discussed in section 3.1, the postmilled phase composition for 2:1:2 and 1:1:1 materials was determined to be primarily $Mg(NH_2)_2$, LiH, and $LiBH_4$ (with remaining MgH_2). The presence of these phases is consistent with spontaneous reactions 1 and 2 or direct reaction 2a, having occurred largely to completion during the milling process. Therefore, unlike the 2:1:1 and 2:0.5:1 composites, reaction 3 is not apparent in the in situ PXRD and IR data for the 1:1:1 (Figures 4c and 5c) and 2:1:2 (Figures 4d and 5d) composites. Instead, the first observed reaction is reversible reaction 4, which begins at approximately 140 °C (on the basis of TPD-MS data in Figure 3) and is evidenced by the formation of product $Li_2Mg(NH)_2$ in PXRD data (30.7° and 51.3° characteristic diffraction lines) and IR data (3178 cm^{-1} observed and reference characteristic N−H stretch).[36,41] As mentioned previously, reaction 3 is an instrumental step in the autocatalytic mechanism, as it serves to provide the kinetically enhancing product seeds for reaction 4. Thus, its absence in the reaction pathway for the 2:1:2 and 1:1:1 composites leads to a decline in kinetic performance at low temperature. In particular, the onset of the first hydrogen desorption step is approximately 15 °C higher. Nevertheless, both the 2:1:2 and 1:1:1 composites have peak desorption temperatures comparable to those of the 2:1:1 and 2:0.5:1 composites, and all four composites exhibit improved kinetics relative to what has been previously observed for reaction 4 in isolation (160 °C onset and 220° peak temperatures for identical TPD-MS experiments).[41]

3.3.2. High-Temperature Hydrogen Release Steps. As was the case for lower temperatures, the 2:1:1 and 2:0.5:1 mixtures exhibit similar reaction pathways at higher temperatures between 200 and 350 °C. This is not unexpected given their nearly identical desorption behavior (one large desorption event) in this temperature range (Figure 3). In particular, in situ PXRD data for 2:1:1 (Figure 4a) and 2:0.5:1 (Figure 4b) reveal a decrease in $Li_2Mg(NH)_2$ and a concomitant increase in Mg_3N_2 and Li_3BN_2 product phases at approximately 300 °C. Characteristic B−N stretches for Li_3BN_2 (1746 and 1682 cm^{-1}, observed; 1737 and 1662 cm^{-1}, reference) were also apparent in variable-temperature IR data. The peak temperature for the second prominent hydrogen release event is also 300 °C (Figure 3), indicating that the above phase changes involve hydrogen as a product.

In contrast to the large single-hydrogen release step observed for the 2:1:1 and 2:0.5:1 composites, the 2:1:2 and 1:1:1 composites display two smaller high-temperature hydrogen release events centered at 225 and 275 °C (Figure 3). At these temperatures, and for both composites, two phase transformations are also apparent from variable-temperature PXRD data (Figure 4c,d). Specifically, at 225 °C a decrease in the $Li_2Mg(NH)_2$ phase is observed with a simultaneous increase in Mg_3N_2; the Li_3BN_2 product phase subsequently emerges at 275 °C. On the basis of these data, we propose the following reaction sequence (reactions 5 and 6) to describe the two-step desorption behavior for the 2:1:2 and 1:1:1 composites:

$$3Li_2Mg(NH)_2 + 6MgH_2 \rightarrow 3Mg_3N_2 + 6LiH + 6H_2 \quad (5)$$

$$3Li_2Mg(NH)_2 + 2LiBH_4 \rightarrow 2Li_3BN_2 + Mg_3N_2 + 2LiH + 6H_2 \quad (6)$$

To further substantiate the above hydrogen desorption reactions, reaction enthalpies (ΔH) and free energies (ΔG) were evaluated using DFT calculations. The calculations indicate that both reactions are exothermic, with enthalpies of −19 kJ/mol of H_2 (reaction 5) and −1 kJ/mol of H_2 (reaction 6) at 250 °C. Likewise, ΔG (T = 250 °C) is negative in both cases [−79 kJ/mol of H_2 (reaction 5) and −61 kJ/mol of H_2 (reaction 6)], further suggesting that the proposed reaction assignment and ordering with regard to temperature is thermodynamically reasonable. Given that both reactions 5 and 6 are exothermic, they should occur immediately after reaction 4 [i.e., once the $Li_2Mg(NH)_2$ is formed]. In practice, however, these reactions appear to require additional heating (above 200 °C) likely resulting from kinetic limitations. On the basis of ref 19, reaction 6 was found to have an activation energy (E_a) of over 180 kJ/mol, which suggests that the kinetic barrier is significant. For the 2:1:1 and 2:0.5:1 composites, H_2, Mg_3N_2, and Li_3BN_2 are formed in a single step, suggesting that only reaction 6 is observed (not reaction 5). The omission of reaction 5 in these composites can be attributed to the fact that both are lacking MgH_2 by this point in their respective reaction sequences (Figure 7). Section 3.4 summarizes these collective findings and offers an explanation for the observed differences in the reaction pathway.

3.4. Reaction Pathway Summary for Postmilled $(LiNH_2)_X-(LiBH_4)_Y-(MgH_2)_Z$ Composites. In sections 3.1−3.3, we presented comprehensive phase identification and hydrogen measurement data in order to derive the stoichiometry-dependent pathway for $(LiNH_2)_X-(LiBH_4)_Y-(MgH_2)_Z$ composites, where $X:Y:Z$ = 2:1:1, 2:0.5:1, 2:1:2, and 1:1:1. Figure 7 summarizes this proposed reaction pathway that includes the six sequential reactions that were revealed earlier (same numbering scheme used) as well as their respective reaction enthalpies (ΔH) calculated at the temperature at which they are experimentally observed. Additionally, Figure 7 depicts the composition of phases for each step and provides insight into the relationship among starting stoichiometry, reaction pathway, and storage properties.

3.4.1. Starting Composition. The top panel of Figure 7 provides the starting composition for each composite. It is evident that the 2:1:1 and 2:0.5:1 composites contain proportionally more $LiNH_2$ and less MgH_2 relative to those of the 2:1:2 and 1:1:1 composites.

3.4.2. Initial Reactions (Milling and Initial Heating to >110 °C). Upon ball milling, the 2:1:1 and 2:0.5:1 starting compositions undergo exothermic reaction 1 ($\Delta H_{300\ K}$ = −12 kJ/mol),[10] producing the quaternary hydride, $Li_4BN_3H_{10}$ (with the remaining $LiBH_4$ and/or MgH_2 starting materials). For the 2:1:2 and 1:1:1 composites, exothermic reactions 1 and 2 (for reaction 2, $\Delta H_{383\ K}$ = −208 kJ/mol) or reaction 2a (ΔH = −74 kJ/mol) occur to completion during milling to produce $Mg(NH_2)_2$, LiH,

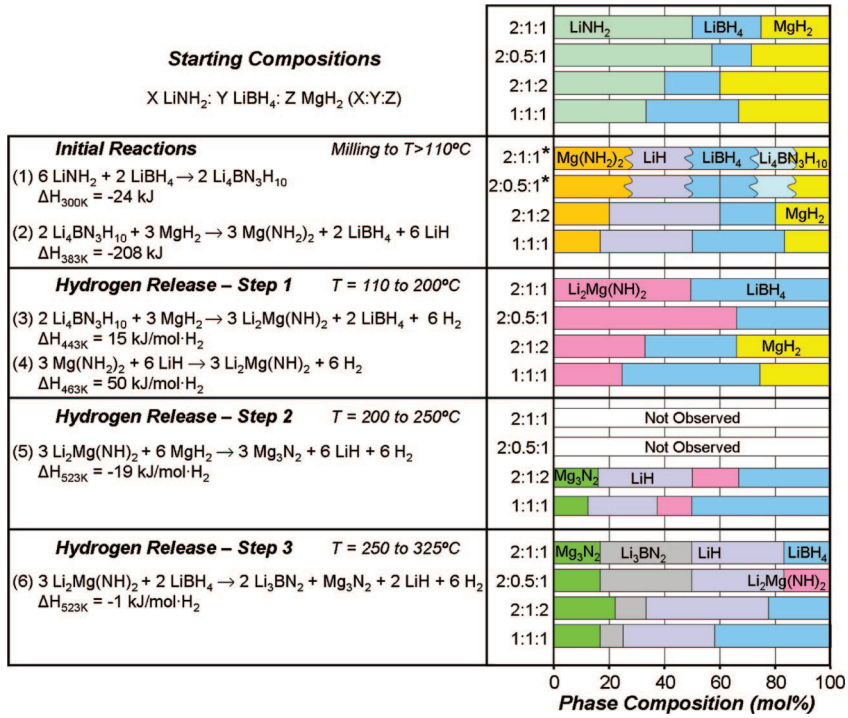

Figure 7. Summary of the proposed reaction pathway for $(LiNH_2)_X$−$(LiBH_4)_Y$−$(MgH_2)_Z$ composites, including reaction enthalpy (ΔH), temperature range, and evolution of phase composition (right panel). The reaction numbers correspond to those used in the text. The asterisks and wavy lines for the 2:1:1 and 2:0.5:1 composites for the initial reactions indicate that the relative amounts of the respective phases are unable to be estimated.

and $LiBH_4$. For the 2:1:1 composite, reaction 2 is only partially observed during milling but is further accessed during initial heating to <110 °C. Reaction 2 is observed only during initial heating for the 2:0.5:1 composite, although it also does not reach completion. Because reaction 2 is only fractionally observed for the 2:1:1 and 2:0.5:1 composites, it is difficult to ascertain the exact amounts of each phase remaining after this step (reflected by the curved lines in Figure 7). Thus, on the basis of PXRD and IR data, upon milling and initial heating (to <110 °C) the 2:1:1 and 2:0.5:1 composites contain a mixture of $Li_4BN_3H_{10}$, $Mg(NH_2)_2$, LiH, $LiBH_4$, and MgH_2 phases, whereas the 2:1:2 and 2:0.5:1 composites contain only $Mg(NH_2)_2$, LiH, $LiBH_4$, and MgH_2.

3.4.3. Hydrogen Release: Step 1 (T = 110−200 °C). For the 2:1:1 and 2:0.5:1 composites, when the temperature surpasses 110 °C, the remaining $Li_4BN_3H_{10}$ and MgH_2 react according to reaction 3 ($\Delta H_{443\ K}$ = 15 kJ/mol of H_2). Unlike reaction 2, reaction 3 produces hydrogen, and, more importantly, generates the $Li_2Mg(NH)_2$ product that serves as preformed nuclei for subsequent reaction 4. Reaction 3, which is instrumental in the kinetics-enhancing autocatalytic mechanism, is not observed for the 2:1:2 and 1:1:1 composites as no $Li_4BN_3H_{10}$ exists. For all composites, reversible hydrogen storage reaction 4 ($\Delta H_{463\ K}$ = 50 kJ/mol of H_2) is observed and is responsible for the majority of hydrogen released at low temperature (2.3−3.6 wt % by 200 °C). Upon completion of reaction 4, the 2:1:1 and 2:0.5:1 composites are comprised solely of $Li_2Mg(NH)_2$ and $LiBH_4$, whereas the 2:1:2 and 1:1:1 composites contain these phases as well as remaining MgH_2.

3.4.4. Hydrogen Release: Step 2 (T = 200−250 °C). The 2:1:2 and 1:1:1 composites, which possess both $Li_2Mg(NH)_2$ and MgH_2, then undergo exothermic hydrogen release reaction 5 ($\Delta H_{523\ K}$ = −19 kJ/mol of H_2). The hydrogen release event centered at 225 °C in the TPD-MS data (Figure 3, bottom panel) is attributed to this reaction for both composites. Reaction 5 is also consistent with the observance of the Mg_3N_2 phase in variable-temperature PXRD data (Figure 4b,c). Because the 2:1:1 and 2:0.5:1 composites do not possess any remaining MgH_2 after reaction 4 (in step 1), step 2 is not observed.

3.4.5. Hydrogen Release: Step 3 (T = 250−325 °C). The final hydrogen release step observed for all four compositions between 250 and 325 °C can be ascribed to exothermic reaction 6 ($\Delta H_{523\ K}$ = −1 kJ/mol of H_2). This reaction occurs to a large extent for the 2:1:1 and 2:0.5:1 composites, as they are composed entirely of $Li_2Mg(NH)_2$ and $LiBH_4$ prior to this stage. Conversely, the 2:1:2 and 1:1:1 composites contain only minor amounts of these reactants, and thus reaction 6 is less prominent in the hydrogen release data (Figure 3). At the completion of step 3, the 2:1:1, 2:1:2, and 1:1:1 composites all contain Mg_3N_2, Li_3BN_2, LiH, and $LiBH_4$. However, the 2:0.5:1 composite is proportionally $LiBH_4$-deficient and thus contains residual $Li_2Mg(NH)_2$ as evidenced in the IR data (Figure 5b) by the imide N−H stretch, which is characteristic for this phase (at 3178 cm^{-1}).

The total observed amounts of hydrogen can be compared with the theoretically expected amount based on the reaction sequence proposed in Figure 7. In particular, the observed (and theoretical) amounts of hydrogen released for the 2:1:1, 2:0.5:1, 2:1:2, and 1:1:1 composites are 8.5 (8.5), 8.6 (8.7), 6.5 (6.6) and 5.7 (5.6) wt %, respectively. On the basis of the Figure 7 reaction summary data, we can aim to refine the reactant ratio such that it would stoichiometrically match the reaction pathway without leaving excess reactants [e.g., for 2:0.5:1 residual hydrogen-containing $Li_2Mg(NH)_2$ remains after reaction 6]. In doing so, the overall and "lower" temperature capacities would be optimized. In particular, the *X:Y:Z* ratio for $(LiNH_2)_X$−$(LiBH_4)_Y$−$(MgH_2)_Z$ should be selected to enable reactions 1–4 to proceed precisely to completion (i.e., without producing excess reactants or products). Additionally, the amount of MgH_2 should be appropriately tuned, so that it would be completely

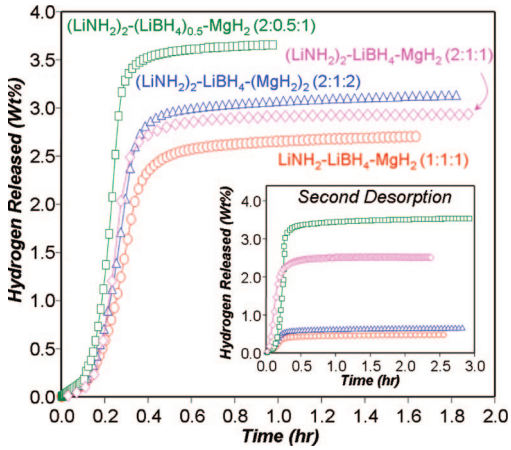

Figure 8. Reversible 180 °C isothermal kinetic hydrogen desorption data (to 1 bar) based on the first desorption cycle for $(LiNH_2)_X-(LiBH_4)_Y-(MgH_2)_Z$ composites, where $X:Y:Z = 1:1:1$ (red circles), 2:1:2 (blue triangles), 2:1:1 (pink diamonds), and 2:0.5:1 (green squares). The inset plot depicts data (same color and shape scheme used) for the second desorption cycle after recharging at 180 °C and 150 bar H_2.

consumed via reactions 2 and 3. This enables the desired autocatalytic reaction 3 to occur while simultaneously optimizing the overall capacity. Thus, on the basis of reactions 1 and 6 in Figure 7, the appropriate $X:Y$ ($LiNH_2$:$LiBH_4$) ratio is 3:1, and from reactions 2 and 3, MgH_2 (Z) should be limited to 1.5. Therefore, the composite which stoichiometrically matches reactions 1–4 and 6 is $(LiNH_2)_3-LiBH_4-(MgH_2)_{1.5}$ (3:1:1.5). This composite is predicted to have a 9.2 wt % total capacity with 4.6 wt % corresponding to the first hydrogen release step (i.e., reactions 3 and 4). Indeed this composition was prepared and examined, and kinetic desorption data revealed a 9.1 wt % total capacity with 4.2 wt % hydrogen liberated by 250 °C (Figure S7 of the Supporting Information). Nevertheless, because this composite is relatively amide-rich (i.e., a proportionally higher $LiNH_2$ content), it is not the most favorable with regard to ammonia liberation (Figure S8 of the Supporting Information).

3.5. Reversibility of Postmilled $(LiNH_2)_X-(LiBH_4)_Y-(MgH_2)_Z$ Composites. The low-temperature reversible storage capacity for each $(LiNH_2)_X-(LiBH_4)_Y-(MgH_2)_Z$ composite was determined based on discharge−charge−discharge experiments performed with a Sievert-type PCT apparatus at 180 °C and charging (discharging) at 150 (1) bar. Results for the first and second desorption cycles are shown in Figure 8. For the first discharge, all composites rapidly liberate hydrogen within 0.5 h. The observed amounts of hydrogen released correlate reasonably well with what is expected, on the basis of the Figure 6 reaction pathway through reaction 4. These observed (expected) amounts for the 2:1:1, 2:0.5:1, 2:1:2, and 1:1:1 composites are 2.9 (4.2), 3.7 (4.8), 3.1 (3.3), and 2.7 (2.8) wt %, respectively. More noticeable differences between observed and expected amounts are apparent for the 2:1:1 and 2:0.5:1 composites. This discrepancy can be understood from the TPD-MS in Figure 3 (bottom panel), where the low-temperature hydrogen release event for the 2:1:1 and 2:0.5:1 composites is not complete at 180 °C, the temperature for this reversibility study. The products of this experiment for all composites are consistent with $Li_2Mg(NH)_2$ and H_2 (i.e., through reaction 4 in Figure 7) and are expected to be reversible. Desorption curves for the second cycle (after recharging) are plotted in the inlay of Figure 7. These data reveal that only the 2:1:1 and 2:0.5:1 composites possess low-temperature reversibility with cycle 2 capacities of 2.5 and 3.5 wt %, respectively. Differences between cycle 1 and cycle 2 capacity for the 2:1:1 and 2:0.5:1 composites could stem from the small portion of hydrogen irreversibly released during reaction 3. For the 2:1:2 and 1:1:1 composites, virtually no hydrogen is released after recharging. For example, under identical charging conditions (180 °C and 150 bar H_2), the 2:1:2 composite still contains $Li_2Mg(NH)_2$ (with the remaining MgH_2 and $LiBH_4$), on the basis of PXRD data in Figure S9 of the Supporting Information. Thus, for the 2:1:2 and 1:1:1 composites, recharging the $Li_2Mg(NH)_2$ phase appears to be prevented under a variety of examined recharging temperature−time conditions (i.e., 180−220 °C and 2−48 h at 150 bar). The only obvious difference between the reversible 2:1:1 and 2:0.5:1 and irreversible 2:1:2 and 1:1:1 composites is the presence of the remaining MgH_2 for the latter compositions. Therefore, we infer that this MgH_2 phase either kinetically or thermodynamically inhibits recharging $Li_2Mg(NH)_2$ under the examined temperature−pressure−time conditions. More detailed investigations are necessary to clarify the role of MgH_2 in the recharging process for the 2:1:2 and 1:1:1 composites.

4. Conclusion

In conclusion, we have examined the hydrogen storage properties and reaction pathways of four distinct stoichiometries within the $LiNH_2-LiBH_4-MgH_2$ ternary composite system using a variety of experimental and computational techniques. The key findings of this study are summarized below.

1. Hydrogen desorption temperature: The 2:1:1 and 2:0.5:1 systems release hydrogen in two primary steps beginning at 140 °C (step 1) and 250 °C (step 2). Conversely, desorption in the 2:1:2 and 1:1:1 composites occurs in three apparent steps with temperature onsets of 155 °C (step 1), 200 °C (step 2), and 250 °C (step 3).

2. Total hydrogen capacity: For temperatures up to 370 °C, the 2:0.5:1 stoichiometry releases the most hydrogen (8.6 wt %), followed closely by the 2:1:1 system with 8.5 wt %. The 2:1:2 and 1:1:1 systems release 6.6 and 5.6 wt %, respectively.

3. Ammonia release: During desorption, ammonia is present at negligible levels for all composites with the exception of the 2:0.5:1 system, which releases considerably more.

4. Reversibility: Only the 2:1:1 and 2:0.5:1 systems exhibit significant low-temperature reversibility with 2.5 and 3.5 wt %, respectively, observed after the second desorption cycle at 180 °C.

5. Reaction mechanism: As expected, all stoichiometries follow the same initial low-temperature reaction pathway, suggesting that the initial pathway is independent of stoichiometry. However, differences in the respective pathways begin to emerge at higher temperatures. At elevated temperatures, the initial stoichiometry (coupled with the degree to which prior reactions have run to completion) determines whether a specified compound is present and is therefore available as a potential reactant. For example, seeding reaction 3 is not present in the 2:1:2 and 1:1:1 systems because by this stage all of the $Li_4BN_3H_{10}$ has been consumed in reaction 2. Additionally, reaction 5 between $Li_2Mg(NH)_2$ and MgH_2 is only observed for 2:1:2 and 1:1:1 composites, which still possess MgH_2 at this stage.

6. Optimal stoichiometry: An optimal stoichiometry of 3:1:1.5 is suggested on the basis of the proposed reaction pathway (Figure 7) and is found to have a high capacity (9.1 wt % total) and low onset temperature for desorption (140 °C). However, ammonia is detected as a desorption byproduct.

Supporting Information Available: Infrared (IR) spectra and powder X-ray diffraction (PXRD) characterization data at

110 °C, ammonia signals from TPD-MS data, and raw variable-temperature PXRD data for all composites (1:1:1, 2:1:2, 2:1:1, and 2:0.5:1). Kinetic desorption data and ammonia signal from TPD-MS data for 3:1:1.5 composite. PXRD pattern for re-charged 2:1:2 composite. This material is available free of charge via the Internet at http://pubs.acs.org.

References and Notes

(1) Crabtree, G. W.; Dresselhaus, M. S.; Buchanan, M. V. *Phys. Today* **2004**, *57*, 39.

(2) Targets for On-Board Hydrogen Storage Systems, 2007. U.S. Department of Energy Web site.http://www1.eere.energy.gov/hydrogenandfuelcells/storage/pdfs/targets_onboard_hydro_storage.pdf (accessed, July 11, 2008).

(3) Züttel, A.; Rentsch, S.; Fisher, P.; Wenger, P.; Sudan, P.; Mauron, P.; Emmenegger, C. *J. Alloys Compd.* **2003**, *356*, 515.

(4) Züttel, A.; Wenger, P.; Rentsch, S.; Sudan, P. *J. Power Sources* **2003**, *118*, 1.

(5) Nakamori, Y.; Li, H.; Miwa, K.; Towata, S.; Orimo, S. *Mater. Trans.* **2006**, *47*, 1898.

(6) Bogdanović, B.; Schwickardi, M. *J. Alloys Compd.* **1997**, *253*, 1.

(7) Orimo, S.; Nakamori, Y.; Eliseo, J. R.; Züttel, A.; Jensen, C. M. *Chem. Rev.* **2007**, *107*, 4111.

(8) Vajo, J. J.; Skeith, S. L. *J. Phys. Chem. B* **2005**, *109*, 3719.

(9) Reilly, J. J.; Wiswall, R. H. *Inorg. Chem.* **1968**, *7*, 2254.

(10) Siegel, D. J.; Wolverton, C.; Ozoliņš, V. *Phys. Rev. B* **2007**, *76*, 134102.

(11) Yang, J.; Sudik, A.; Wolverton, C. *J. Phys. Chem. C* **2007**, *111*, 19134.

(12) Sun, D.; Srinivasan, S.; Kiyobayashi, T.; Kuriyama, N.; Jensen, C. M. *J. Phys. Chem. B* **2003**, *107*, 10176.

(13) Pinkerton, F. E.; Meyer, M. S.; Meisner, G. P.; Balogh, M. P. *J. Alloys Compd.* **2007**, *433*, 282.

(14) Pinkerton, F. E.; Meisner, M. M.; Balogh, M.; Kundrat, M. *J. Phys. Chem. B* **2005**, *109*, 6.

(15) Aoki, M.; Miwa, K.; Noritake, T.; Kitahara, G.; Nakamori, Y.; Orimo, S.; Towata, S. *Appl. Phys. A: Mater. Sci. Process.* **2005**, *80*, 1409.

(16) Chater, P. A.; Anderson, P. A.; Prendergast, J. W.; Walton, A.; Mann, V. S. J.; Book, D.; David, W. I. F.; Johnson, S. R.; Edwards, P. P. *J. Alloys Compd.* **2007**, *446*, 350.

(17) Luo, W. *J. Alloys Compd.* **2004**, *381*, 284.

(18) Wu, G.; Xiong, Z.; Liu, T.; Liu, Y.; Hu, J.; Chen, P.; Feng, Y.; Wee, A. T. S. *Inorg. Chem.* **2007**, *46*, 517.

(19) Yang, J.; Sudik, A.; Siegel, D. J.; Halliday, D.; Drews, A.; Carter, R. O., III.; Wolverton, C.; Lewis, G. J.; Sachtler, J. W. A.; Low, J. J.; Faheem, S. A.; Lesch, D. A.; Ozonliņš, V. *Angew. Chem., Int. Ed.* **2008**, *47*, 882.

(20) Sudik, A.; Yang, J.; Halliday, D.; Wolverton, C. *J. Phys. Chem. C* **2008**, *112*, 4384.

(21) Hu, J.; Liu, Y.; Wu, G.; Xiong, Z.; Chua, Y.-S.; Chen, P. *Chem. Mater.* **2008**, *20*, 4398.

(22) Lewis, G. J.; Sachtler, J. W. A.; Low, J. J.; Lesch, D. A.; Faheem, S. A.; Dosek, P. M.; Knight, L. M.; Halloran, L.; Jensen, C. M.; Yang, J.; Sudik, A.; Siegel, D. J.; Wolverton, C.; Ozoliņš, V.; Zhang, S. *J. Alloys Compd.* **2007**, *446*−*447*, 355.

(23) Kresse, G.; Furthmüller, J. *Phys. Rev. B* **1996**, *54*, 11169.

(24) Blöchl, P. E. *Phys. Rev. B* **1994**, *50*, 17953.

(25) Perdew, J. P.; Chevary, J. A.; Vosko, S. H.; Jackson, K. A.; Pederson, M. R.; Singh, D. J.; Fiolhais, A. C. *Phys. Rev. B* **1992**, *46*, 6671.

(26) Sorby, M. H.; Nakamura, Y.; Brinks, H. W.; Ichikawa, T.; Hino, S.; Fujii, H.; Hauback, B. C. *J. Alloys Compd.* **2007**, *428*, 297.

(27) Partin, D. E.; Williams, D. J.; O'Keeffe, M. *J. Solid State Chem.* **1997**, *132*, 56.

(28) Rijssenbeek, J.; Gao, Y.; Hanson, J.; Huang, Q.; Jones, C.; Toby, B. *J. Alloys Compd.* **2008**, *454*, 233.

(29) Siegel, D. J.; Wolverton, C.; Ozoliņš, V. *Phys. Rev. B* **2007**, *75*, 014101.

(30) Wolverton, C.; Siegel, D. J.; Akbarzadeh, A. R.; Ozoliņš, V. *J. Phys.: Condens. Matter* **2008**, *20*, 064228.

(31) Chater, P. A.; David, W. I. F.; Johnson, S. R.; Edwards, P. P.; Anderson, P. A. *Chem. Commun.* **2006**, (23), 2439.

(32) Luo, W.; Sickafoose, S. *J. Alloys Compd.* **2006**, *407*, 274.

(33) Yang, J.; Sudik, A.; Wolverton, C. *J. Alloys Compd.* **2007**, *430*, 334.

(34) While not performed, it is anticipated that if the 2:1:1 and 2:0.5:1 composites were held at <110°C for a longer period of time, reaction 2 would occur to completion, leaving no residual $Li_4BN_3H_{10}$.

(35) The disparity in temperature between kinetic desorption (Figure 3, top) and TPD-MS (Figure 3, bottom) data can be attributed to the pressure difference during data acquisition, 1 bar static for kinetic desorption and 100 sccm flowing Ar for TPD-MS experiments.

(36) Chen, P.; Xiong, Z.; Yang, L.; Wu, G.; Luo, W. *J. Phys. Chem. B* **2006**, *110*, 14221.

(37) Meisner, G. P.; Scullin, M. L.; Balogh, M. P.; Pinkerton, F. E.; Meyer, M. S. *J. Phys. Chem. B* **2006**, *110*, 4186.

(38) Luo, W.; Stewart, K. *J. Alloys Compd.* **2007**, *440*, 357.

(39) Goubeau, V. J.; Anselment, W. *Z. Anorg. Allg. Chem.* **1961**, *310*, 248.

(40) Xiong, Z.; Wu, G.; Hu, J.; Chen, P. *Adv. Mater.* **2004**, *16*, 1522.

(41) Sudik, A.; Yang, J.; Halliday, D.; Wolverton, C. *J. Phys. Chem. C* **2007**, *111*, 6568.

JP807270Y